Chapter 5

Actinide Accommodation in Pyrochlores

Some of this work has previously been published in Philosophical Magazine [3]

5.1 Introduction

As mentioned in the general literature review (section 2.3.5), there has been significant interest in the use of ceramics for the immobilisation of nuclear waste and actinides in particular. Of these it was also mentioned in chapter 4 that fluorite related materials including fluorite solid solutions $Er_2Zr_2O_7$ (i.e. Er_2O_3 - ZrO_2) and $Er_2Ce_2O_7$ [132, 232] have been shown to have remarkable resistance to amorphisation under "heavy ion" irradiation. Similar results

were found for the pyrochlore $Gd_2Zr_2O_7$ [35]. On the other hand, Lian *et al.* showed that $La_2Zr_2O_7$ pyrochlore "will undergo" amorphisation [233], however it is still a radiation tolerant material when compared with most ceramics.

If these oxide materials are to be used as host phases for actinides it is important to understand how the $A_2B_2O_7$ compounds might incorporate large actinide ions in their structure. It would also be interesting to know how this varies as a function of composition. Thus, using atomic scale computer simulation, the solution energies of uranium and plutonium in both trivalent and tetravalent states have been predicted within pyrochlore oxides. Results will be reported in the form of contour maps that present solution energy as a function of composition (contour maps will be explained in section 5.3).

5.2 Literature Review

5.2.1 Background and History

Pyrochlore materials and other fluorite related ceramics have generated significant interest for the purpose of immobilising actinides and other nuclear wastes [30–37, 61, 77, 232–247]. The crystallography and phase stability of pyrochlore compounds were discussed in chapter 4 and it was also mentioned that there is a huge range of possible pyrochlore compositions. Chakoumakos [248] reports that there have been at least 440 synthetic compounds with the pyrochlore structure alone and pyrochlore minerals have been found

in rock formations in locations around the world [31]. Naturally-occurring pyrochlores have been found containing both uranium and thorium [31, 78, 249] and Lumpkin [78] reports that natural pyrochlores have been found containing up to 30 wt% UO_2 and 9 wt% ThO_2. It is therefore unsurprising that pyrochlore and related structures have been present in the earliest nuclear waste forms [31].

During the 1980's, much of the research into the SYNROC wasteform was performed [78] and this research gained more importance in the 1990's when options to immobilise the plutonium from dismantled nuclear weapons were required [31]. With the immobilisation of weapons Pu in mind, the U.S.A. settled on a collection of titanate phases very similar to the original SYNROC composition mainly due to its proven chemical durability [31]. As mentioned in section 2.3.5 the SYNROC phase designed to accommodate most of the actinides (and Pu in particular) was zirconolite ($CaZrTi_2O_7$). In their study into Np and Pu doping of zirconolite, Begg *et al.* [45] found when the zirconolite phase is doped with approximately 20 mole% PuO_2 a mixture of $Ca_{0.95}Pu_{0.23}Zr_{0.87}Ti_{1.93}O_7$ zirconolite and $Ca_{0.95}Pu_{0.90}Zr_{0.28}Ti_{1.84}O_7$ pyrochlore was formed. It is clear that this pyrochlore can accept much higher loadings of Pu than the zirconolite (this case shows nearly a four fold increase). A similar result was found in earlier work when a number of studies where performed doping zirconolite with ^{238}Pu (half life 87.7 years) in order to assess it's stability under α-decay (see references 42-46 in [31]). The samples doped with 4 mole% $^{238}PuO_2$ stayed monoclinic but samples doped with more than 8 mole% $^{238}PuO_2$ were reported to form a "cubic zirconolite" phase. This was subsequently shown to be a defective pyrochlore structure

(reference 47 in [31]).

5.2.2 Previous Work on the Solubility of Actinides in Pyrochlore

5.2.3 Solution Studies

The issue of actinide accommodation has already been tested experimentally in lanthanum zirconate by [240, 242] through the preparation of compositions $[La_{1-x}Pu_x]_2 Zr_2O_{7+y}$ compositions with x ranging from 0 ($La_2Zr_2O_7$) to 1 ($Pu_2Zr_2O_7$). Kulkarni *et al.* [242] produced samples with intermediate values of x at 0.25 and 0.5. This was achieved by mixing oxide powders and graphite (to reduce the Pu^{4+} to Pu^{3+}) and heating to 1400 °C in a helium atmosphere. They found that all of the compounds formed cubic pyrochlore with the lattice parameter decreasing linearly with increasing Pu content. This shows complete solid solubility of Pu in $La_2Zr_2O_7$ [242]. These authors also described $Pu_2Zr_2O_7$ [242] but this will be discussed in the next section.

Yamazaki *et al.* [240] examined the same system in greater depth. They sampled x from 0 to 0.3 in steps of 0.05 and 0.3 to 1.0 in steps of 0.1 making it possible to be more certain as to the extent of solubility. They too opted for the powder processing route but heated the mixtures in 3 different atmospheres, a vacuum, an 8% hydrogen-helium atmosphere and air, all at 1500 °C. The samples formed in the hydrogen-helium atmosphere were further treated at 1700 °C for 5 hours in order to reduce the plutonium valence.

Looking at the air sintered samples first, Yamazaki *et al.* [240] found that the lattice parameter only increases linearly with increasing Pu content until x=0.1. Beyond this point further increasing the Pu content has no effect on the lattice parameter so they determine the solubility limit for air sintered samples to be 10 mole %. From this and the fact that Ce (a close chemical analogue for Pu) is tetravalent when heated in air this low value was used by the authors to justify that the majority of the Pu in the material was tetravalent. They also found that an air heated solution consisting of 80 mole % Pu formed a single fluorite phase and the 100% Pu sample showed a mixture of a fluorite phase and tetragonal zirconia. The vacuum heated samples showed a solution limit at about 35 mole % and further increases in Pu content resulted in the formation of a two phase fluorite - pyrochlore region. This indicates that under vacuum conditions, a significant amount of the Pu^{4+} was reduced to Pu^{3+} but the relative amounts could not be confirmed by the authors. The region from 80 mole to 100 mole % showed only a single fluorite phase. The samples heated under the most reducing conditions agree with the results from Kulkarni *et al.* [242] in that under these conditions, the lattice parameter continues to decrease with increasing Pu content throughout the entire range showing a single pyrochlore type phase throughout. They found that samples between 50 and 80 mole % Pu showed a mixture of pyrochlore and a cubic type phase but they surmised that as both end members were pyrochlore the phases in between were likely to be pyrochlore-like phases, however, the characteristic diffraction peaks were weak so this could not be confirmed [240].

Since both studies established that plutonium could exhibit either trivalent

or tetravalent charge states depending on the preparation temperature and pO_2, the solution of both Pu^{3+} and Pu^{4+} will be modelled here. Uranium is considered in both trivalent and tetravalent states as, although U_2O_3 has not been formed experimentally, UO_2 shows considerable hypo-stoichiometry (i.e. UO_{2-x}) and the formation of the sub-stoichiometric oxide could be indicative of the formation of U^{3+}. Details on the derivation of the U^{3+} potential will be discussed in section 5.3.

$[Ln\text{-}Pu]_2Ti_2O_7$ compositions have been fabricated by Shoup *et al.* [36] where Ln = Gd, Er and Lu. Considered as solid solutions of $Pu_2Ti_2O_7$ in $LnTi_2O_7$ the solution limit was considerable in each case with the value for the Lu variant largest at 33 mol% and the value for Gd smallest at 16 mol%.

Previous solution energy simulations have been carried out by Weber *et al.* [234] by substituting Pu^{3+} and Pu^{4+} in the pyrochlore and fluorite forms of $Gd_2Zr_2O_7$. It was found that Pu^{3+} substituted most readily for Gd^{3+} in both structures (-1.00eV/Pu and -1.55eV/Pu respectively). The Pu^{4+} ion was found to be most stable at the Zr^{4+} sites in pyrochlore and fluorite with energies of -0.26eV and -0.45eV.

The accommodation of Pu^{4+} in pyrochlores has also been considered experimentally via a co-doping approach [37]. In this case, the plutonium ions are assumed to occupy A sites with compensation by Ca^{2+} also on A sites. The rationale for this mechanism is provided by the existence of the mineral zirconolite (discussed previously) [41, 78] and the mineral betafite which has the formula $CaUTi_2O_7$ [38]. Natural zirconolites are known to accommodate uranium ions (see section 2.3.5). However, the zirconolite structure is distin-

guished from pyrochlore by the formation of complex ordered layers which also results in the possibility of polymorphs [41]. Also, recently [30] evidence has been published which suggests that while plutonium resides on the A sites as Pu^{3+}, uranium occupies the B site as a U^{5+} ion. This last case was not considered in this study due to time constraints.

Extreme Doping Studies (Formation of $Ac_2B_2O_7$)

While pyrochlores have been shown to accommodate large quantities of PuO_2 or Pu_2O_3, several groups have managed to form pyrochlores with the formula $Ac_2B_2O_7$ where Ac is either Pu, Cf or Am and B is either Ti or Zr [36, 240, 242, 250]. Both Kulkarni *et al.* [242] and Yamazaki *et al.* [240] managed to form $Pu_2Zr_2O_7$. Shoup *et al.* managed to form a monoclinic $Pu_2Ti_2O_7$ which may or may not be isostructural with the monoclinic $La_2Ti_2O_7$ synthesised by Schmalle *et al.* [166] and very recently Sykora *et al.* [250] synthesised both $Am_2Zr_2O_7$ and $Cf_2Zr_2O_7$ for a self irradiation study that will be discussed in more depth later. In their study, Kulkarni *et al.* [242] found that $Pu_2Zr_2O_7$ oxidised easily in air at temperatures below 600 °C to reform in the disordered fluorite structure ($[Pu_{0.5}Zr_{0.5}]O_2$). Repository conditions are likely to be strongly reducing (except for the Yucca Mountain repository in Nevada which will be oxidising [251]). so this transition is unlikely given proper handling of the material but even if it does occur, the volume change caused by this change is very small. The measured a lattice parameter for the pyrochlore as 10.592 Å and the fluorite structure was 5.273 Å [242]; allowing for the fact that both structures are cubic and that the lattice parameter for pyrochlore

is twice the size of the fluorite this corresponds to a volume reduction of 1.3% associated with this transformation. These studies demonstrate an ability for materials with the pyrochlore structure to accommodate high concentrations of actinides.

5.2.4 Irradiation Effects in Pyrochlores

General radiation effects and radiation induced damage in wasteforms were discussed in section 2.3.6. The methods used to study the effects of α-decay in wasteform materials using experimental techniques include doping with short lived actinides such as ^{238}Pu or ^{244}Cm (half-lives 87.7 and 18.1 years respectively), ion-beam irradiation (implantation) studies and studying natural analogues. Computer simulation techniques generally examine the behaviour of a single decay event using molecular dynamics models. A review of irradiation studies on pyrochlore systems including both experimental and theoretical methods will now be presented.

Doping with Short Lived Actinides

By doping with short lived actinide species, it is possible to accelerate the dose rates by several orders of magnitude over that which a real wasteform will experience [31] and it allows simulation of damage to the bulk of the material rather than just the a few tens of microns away from the surface [252] as with ion-beam studies. By accelerating the dose rate in this manner it is possible to simulate the cumulative dose that a wasteform would experi-

ence over hundreds or thousands of years in time periods short enough for experimental observations to be carried out. This type of study is the most realistic way of simulating radiation damage in prospective wasteforms but only a few places in the world are capable of performing such studies due to the equipment required to handle such materials.

Strachan *et al.* started a series of experiments in 1999 in which they doped a series of titanate ceramics with ^{238}Pu and ^{239}Pu [253] and stored them at a range of temperatures from ambient to 250 °C until the ^{238}Pu sample became fully amorphous or the damage reached saturation point [252–254]. The ceramics tested are the three phases that comprise the U.S.A.'s wasteform for weapons plutonium not suitable for conversion to MOX fuel: a $CaUTi_2O_7$ pyrochlore, a $CaZrTi_2O_7$ zirconolite and a UTi_2O_6 brannerite compound. The samples were synthesised with a Pu content roughly equal to 10 wt%, with the exception of the brannerite phase which did not form and was not considered further.

Once synthesized, all samples were analysed using X-Ray Diffraction (XRD) patterns, density measurements and photographs for later comparison and an initial 3 day leach test was carried out [253]. Results from this test for the ^{238}Pu doped samples showed relatively high but comparable leach rates for both the pyrochlore and the zirconolite. The authors point out that these samples were newly formed at this point and this may cause strange results due to unreacted materials and grain boundary phases [253]. In the most recent paper from the same group [252], they attribute this initial high rate to radiolysis effects on the leachant that caused enhanced dissolution.

This work was continued in 2001 by Strachan *et al.* [254]. At this point, due to differences in composition, the pyrochlore phase had received a dose of about 3×10^{18} α-decays per gram and the zirconolite had received 2×10^{18} α-decays per gram. For these two compounds, the authors report that the pyrochlore should be almost completely amorphous and the zirconolite should be 80% amorphous [254]. While not strictly comparable as these materials are being examined for the immobilisation of actinides, it was mentioned in table 2.3 that a nuclear waste glass would experience 1×10^{18} α-decays per gram after 1,000,000 years. It was found, as expected, that all samples containing ^{238}Pu show some volume change, the density reduction is reported for the pyrochlore to be 8% and the zirconolite showed a more considerable density reduction of 15% even though it has received a lower dose [254]. These values are for the room temperature specimens.

XRD patterns of the room temperature samples showed that after one year in a titanate ceramic doped with ^{238}Pu the pyrochlore phase had become amorphous. The zirconolite constituent seemed to be more resilient but it had experienced a lower dose [254]. As will be mentioned later, it has been noted that there is considerable variation in the amorphisation resistance in the pyrochlore system and the titanate system is more susceptible then the zirconate system so a different composition may not have amorphised. However, for this system, after this time, the authors report the only crystalline phases present in the pyrochlore material were from a TiO_2 rutile, HfO_2 solid solution. They attribute this to the low solubility of PuO_2 in rutile so that the number of ^{234}U recoil atoms that reach these phases is lower than for the sample as a whole.

In the same report, the authors give the results for a 350-day dissolutions study on the ^{239}Pu-doped samples and 3-day dissolution studies on the ^{238}Pu-doped samples (longer was not possible due to radiolysis of the water). Details of the leaching study can be found in [254]. In summary, comparing the rates for the ^{239}Pu sample with the ^{238}Pu-doped sample shows that the radiation damaged sample showed a leach rate about 1000 times faster for the release of Pu and 700 times for the U [254]. While these seem alarmingly large changes, the leach rates are still on the order of milligrams per square metre per day.

In the concluding paper published recently by the same group [252] where they repeated some of their earlier work, they found that there is virtually no difference (within experimental uncertainties) between the samples doped with ^{238}Pu and ^{239}Pu and concluded that even though the samples become amorphous, there is no change in the dissolution rate caused by radiation damage. They calculated the final dose that the ^{238}Pu doped ceramic has received to be 7.5×10^{18} α-decays per gram and that for a material doped with 10 wt% ^{239}Pu this would correspond to a period of 970 years in the repository. After this period, they predict a volume increase of about 7% due to amorphisation but no cracking or degradation of the samples was observed. They go on to state that either the pyrochlore or the zirconolite would be good candidates for the immobilisation of Pu.

Another actinide doping study was mentioned earlier in the section regarding the formation of the americium and californium zirconate pyrochlores by Sykora *et al.* [250]. They formed "very small" samples by mixing stoichio-

metric quantities of zirconyl nitrate with either $CfCl_3$ or AmO_2. The samples were dried and calcined at temperatures of up to 1500 °C. The authors found that the californium pyrochlore formed without any problems in air but the americium required a 4% hydrogen in argon atmosphere to prevent it oxidising to Am^{4+} [250]. Sykora *et al.* [250] performed XRD on the samples after 1 month and then after 2 years of self irradiation. After a month, both materials were still crystalline. The californium isotope (^{249}Cf) used in this study had a shorter half life (351 years) than the americium isotope (mass number or half-life not given) and the authors report the final analysis of the americium pyrochlore as work in progress [250]. Both of the samples were shown to exhibit slight swelling of the lattice parameter during the early part of the study which the authors surmised was due to either the accumulation of point defects from α-decay, the inclusion of helium in the matrix or a combination of both. The californium compound lost the characteristic pyrochlore diffraction lines after 6 months of self irradiation (a corresponding dose of 1.17×10^{24} α-decay per gram [250]). While the material no longer exists in the pyrochlore structure, Sykora *et al.* [250] report that the diffraction pattern was indicative of a solid solution of mixed dioxides or an oxygen deficient fluorite structure but not amorphous like the titanate systems discussed earlier. The pyrochlore structure can be regained by reheating [250]. They found similar results for the americium pyrochlore and the ability to resist amorphisation at such high doses whilst incorporating such large proportions of actinide species shows that the resistance to amorphisation from α-decay is a hugely variable parameter in the pyrochlore compositional field.

Ion Beam Irradiation Studies

By using an accelerated beam of heavy ions, it is possible to simulate similar damage levels to what would correspond to several thousand years of α-decay in a real wasteform in a few days [31]. Ion beam irradiation facilities are far more widespread than laboratory facilities equipped to handle highly radioactive species such as ^{238}Pu [252–254]. The problems with ion beam irradiation studies is that they can only damage a small region close to the surface (a few tens of microns) and they only produce damage that is similar to alpha decay, although, in their review, Ewing *et al.* [31] report that results are consistent with highly damaged ^{244}Cm doped samples. Ewing *et al.* go on to say that ion-beam irradiation studies can provide a reasonable representation of the worst case effects of radiation damage on chemical durability over the intervals of interest for actinide containing wasteforms [31].

There have been numerous ion-beam irradiation studies on pyrochlores and the related disordered fluorite structure [233, 235, 246, 247, 255–263]. The disordered fluorite structure is relevant here due to the fact that many pyrochlores undergo a disordering transformation under irradiation to fluorite [247].

Examining the latter stages of radiation damage first, Sickafus *et al.* [132,232] demonstrated that fluorite solid solutions (i.e. $Er_2Zr_2O_7$ and $Er_2Ce_2O_7$), showed remarkable resistance to amorphisation under heavy ion irradiation. In their study, Sickafus *et al.* [132] bombarded both the $Er_2Ti_2O_7$ pyrochlore and the $Er_2Zr_2O_7$ disordered fluorite with 350-keV Xe^{++} ions at the temperature of 120 K in order to inhibit recovery processes. While the titanate

system became amorphous at a fluence of 1×10^{15} Xe ions per cm^2, the disordered fluorite system remained crystalline until the experiment was ended at a fluence of 1×10^{16} Xe ions per cm^2.

In the pyrochlore system, ion-beam radiation studies have tended to concentrate on the titanates, which tend to readily undergo amorphisation at relatively low doses. The zirconate systems require significantly higher doses to become amorphous or undergo a disordering transformation to form a defective fluorite structure which may or may not become amorphous. Some of the ion-beam irradiation studies will now be reviewed in greater depth.

Wang and coworkers [263] compared the resistance of a $Gd_2Ti_2O_7$ pyrochlore and a $CaZrTi_2O_7$ zirconolite by bombarding them whilst simultaneously monitoring the system using Transmission Electron Microscopy (TEM). They bombarded the materials with 3 types of ion beam over a wide range of temperatures between room temperature and 1000 °C. The three types of ion beam were 1.5 MeV Xe^+, 1 MeV Kr^+ and 0.6 MeV Ar^+ [263] and the dose rate was 8.5×10^{11} ions per cm^2 per second. The authors found that the $Gd_2Ti_2O_7$ pyrochlore gradually disordered into the disordered fluorite structure and partially amorphised until the transformation was complete when the entire system became amorphous. At room temperature, this occurred at a fluence of 7.57×10^{14} ions per cm^2. Wang *et al.* concluded that the gradual and concurrent amorphisation and fluorite transformation originated from different regions of the cascades caused by the bombardment. The central core of the cascade where damage is greatest becomes amorphous, whilst the outer regions are merely disordered forming a fluorite structure [263]. The

zirconolite that was also studied became amorphous at a slightly lower dose of 6×10^{14} ions per cm^2 but it showed a more complicated structural transition. Wang *et al.* [263] found that after a fluence of about 2×10^{14} ions per cm^2 a partially cation disordered pyrochlore had formed. This disappears at twice the fluence and only a disordered fluorite structure is left. This then slowly amorphises until it becomes fully amorphous at 6×10^{14} ions per cm^2 [263].

Begg *et al.* [260] also considered the ion irradiation of titanate pyrochlores but they also looked into the effect that amorphisation has on the dissolution rates. This group also use *in-situ* TEM to monitor the amorphisation process and they used 0.6 MeV Bi^+ ions as the bombarding species. The pyrochlores studied included the Gd, Y, Sm and Lu titanates. The effect of temperature on the was also considered in the range 20 to 1000 K so that temperature variation of the critical irradiation dose could be determined (as in the previous study by Wang *et al.* [263]). They found that there is no significant effect on the critical dose by varying the A cation with all the titanate pyrochlores tested having a critical temperature somewhere close to 975 °C [260]. They also found that all of these titanate pyrochlores undergo room temperature amorphisation at a low dose (about 0.18 dpa in this case). Like the previous study [263] they found that the pyrochlore showed a combined amorphisation and transformation to fluorite until amorphisation was complete.

Moving on to the leach results from the same study; samples 10mm × 10mm × 1mm were prepared and polished to a 0.5μm finish. These were then

irradiated on both large faces to a fluence of 5 ions per nm^2 (using 2 MeV Au^{++} ions). This produced an amorphous layer about 380 nm thick on each sample [260]. After 15 days at a temperature of 90 °C and at pH 2 the dissolution rates for Gd and Ti ions from the $Gd_2Ti_2O_7$ sample were 15 times higher than for the undamaged sample. After 21 days, the dissolution rates dropped slightly to a factor of 10 higher for Gd and 2 for Ti ions. The much slower rate for Ti dissolution was found to be due to the formation of anatase (TiO_2) on the surfaces of the damaged specimens. They noted that this order of magnitude change in dissolution rate upon amorphisation is consistent with previous work on ^{244}Cm doped $Gd_2Ti_2O_7$ [260]. The $Y_2Ti_2O_7$ sample showed similar results for the Ti dissolution rate but no change in the Y dissolution rate although the rate of dissolution of Y from the crystalline sample was reported as equivalent to the amorphous dissolution rate of Gd. The $Lu_2Ti_2O_7$ sample showed enhanced dissolution rates of a factor of 5 after 9 days and at the end of the study this had reduced to a factor of 3. The Ti leach rates from the same sample initially peaked at 20 times higher than the crystalline sample and ended up 9 times greater [260]. In general, leach rates increase substantially upon amorphisation and thus compositions that do not amorphise are preferable.

Moving from titanate pyrochlores to the zirconates, Lian *et al.* studied the ion-irradiation effects on $A_2Zr_2O_7$ pyrochlores where A is La, Nd, Sm or Gd using by 1.5 MeV Xe^+ ions and performing *in-situ* TEM observations [233, 257]. They also performed a 200 keV Ti ion implantation on bulk $Gd_2Zr_2O_7$ to a very high dose of 1×10^{17} ions per cm^2 and studied the evolution of the microstructure using cross sectional TEM. Lian *et al.* found that all

of the zirconate pyrochlores underwent a disordering transformation to the disordered fluorite structure as in the titanate system. Of all the samples tested only $La_2Zr_2O_7$ showed similar behaviour to the titanates. All the others slowly disordered forming a disordered fluorite structure. Even though $La_2Zr_2O_7$ became amorphous, it was significantly more resistant than the titanates studied by Begg *et al.* [260], only amorphising at room temperature at a dose of 5.5 dpa (compared with 0.18 dpa). All the other zirconates remained crystalline defect fluorites even with irradiation temperatures as low as 25 K even after doses of 7 dpa. The ion implanted bulk sample of remained $Gd_2Zr_2O_7$ crystalline fluorite and the calculated dose in the surface region was about 100 dpa [233]. In this study they compare $Gd_2Zr_2O_7$ with the results from Sickafus *et al.* [127] where they discuss the amorphisation resistance of radiation induced cubic zirconia (pure monoclinic zirconia that has become cubic upon ion irradiation) which has been shown to resist amorphisation to 680 dpa.

Molecular Dynamics Studies

Molecular dynamics (MD) simulations are able to simulate a single cascade, something that is usually very difficult to observe. Conventional MD calculations, however, are very limited in terms of the timescale of the simulations with current computing resources generally proceeding up to some tens of picoseconds.

There have been two MD simulations studied recently that have attempted to model both the effect of displacement cascades caused by α-recoil atoms

[264,265] and one that considered the global amorphisation of $La_2Zr_2O_7$ [266]. Purton and Allan [264] ran five calculations with PKA (primary Knock-on Atom) energy less than 10 keV and 2 calculations between 10 and 20 keV in both $Gd_2Ti_2O_7$ and $Gd_2Zr_2O_7$. They found that the number of defects was significantly greater in the titanate case and that there was a significant difference in the configuration of the final defects. They stated that the $Gd_2Zr_2O_7$ cascade had an elongated or cylindrical shape and had a very ordered structure and that many of the oxygen ions become associated with the 8a lattice position in the pyrochlore space group and thus became more fluorite like [264] in agreement with experimental studies. Contrasting with this, the $Gd_2Ti_2O_7$ pyrochlore was reported to have a more ellipsoidal structure and have an amorphous core with no obvious ordering. Purton and Allan attributed this difference to the ability of $Gd_2Zr_2O_7$ to accommodate disorder and show increased ionic conductivity over $Gd_2Ti_2O_7$.

Chartier *et al.* have performed an in depth MD study of the $La_2Zr_2O_7$ system [265] in which they analysed many properties in order to ensure their potentials would reproduce the system as well as possible. Before considering recoil events, they calculated the average and the minimum displacement energies for all the species (averages calculated over 14 different directions) Oxygen has the lowest average displacement energy of 38 eV, next comes La with 153 eV followed by 188 eV for the Zr. They define the displacement energy to be the minimum kinetic energy transferred from the PKA to an atom along a given crystallographic direction yielding a Frenkel pair [265].

The recoil event simulations of Chartier *et al.* were set up in a simulation cell

containing about 152000 atoms (consisting to an $8 \times 8 \times 8$ supercell). One of the Zr^{4+} atoms at approximately $(\frac{1}{4}, \frac{1}{4}, \frac{1}{4})$ in the supercell was replaced with a U^{4+} which was then equilibrated to 350 K under constant pressure conditions. The cascade simulations were then run using periodic boundary conditions under constant volume conditions with a PKA energy of 6 keV in the [111], [322], [211] and [221] directions. They found that the peak number of displacements occurs at about 30fs into the cascade where 807 oxygen ions, 171 lanthanum ions and 91 zirconium ions have been displaced. A rapid recovery stage was then observed until about 900fs at which they observed about 40% of the displaced ions had returned to their previous or to equivalent lattice sites. This was then followed by a much slower process where roughly 10% of the remaining oxygen interstitial ions migrated back to lattice sites [265]. The authors note that they saw oxygen ions at the 8a site returning to the 48f site up to 4ps into the cascade although no more occupancies were noted until the end of the cascade after 7.5ps. They report that all directions produced similar effects but that the [111] and [322] directions produced 20% more defects. They attribute this to the fact that the first atom hit by the PKA is different for the two classes of direction yielding different sub-cascades [265]. They also note that no cation interstitial ions remain at the end of the cascade, only antisite defects. They go on to conclude that during isolated cascade events $La_2Zr_2O_7$ retains its crystallinity with over 90% of the initially displaced atoms returning to equivalent sites after 1ps and that the average number of residual interstitial ions produced by a 6 keV U PKA is about 70.

Chartier *et al.* also attempted to used molecular dynamics techniques to simulate disorder induced amorphisation in $La_2Zr_2O_7$ [266]. In order to achieve this they first tested their system to see if they could produce a disordered fluorite system. This required a cell containing 704 atoms initially in a pyrochlore structure in which half the cations were randomly swapped into antisite configurations and then the system was allowed to relax using MD for 18 ps. No deliberate oxygen disorder was introduced [266]. During this period, the oxygen ions spontaneously moved and generated a disordered fluorite system.

In order to explore the transition of the pyrochlore to the disordered fluorite, Chartier *et al.* used 140 different configurations of the cell just described containing different numbers of cation antisite defects ranging from 0 to 100%. They noted that disorder on the anion sublattice follows the cation sublattice on almost a 1:1 ratio and therefore conclude that disorder on the cation sublattice directly drives the anion disordering process [266]. In order to simulate the pyrochlore to fluorite transformation under more realistic radiation damage processes, Chartier *et al.* introduced different random concentrations (up to 16%) of Frenkel pairs in the lattice, and this was carried out in a ratio of 2:1 La to Zr Frenkel pairs in order to reproduce the numbers seen in previous MD simulations [265]. They estimate that complete transformation to the fluorite system will occur at a concentration of 20%. To go on to model the amorphisation process, Chartier *et al.* introduced small numbers of Frenkel pairs into the disordered fluorite cell under constant pressure and constant volume simulations. Under the constant volume regime, they found that no matter how many Frenkel pairs were introduced, no amorphisation occurred

but under constant pressure conditions, an introduction of 10% Frenkel pairs (equal numbers of cations) results in an amorphous transition [266]. This difference between the constant volume and constant pressure regimes seems logical as experimentally, there is an associated volume change upon amorphisation for the pyrochlores [254]. Chartier *et al.* [266] went on to conclude that $La_2Zr_2O_7$ transforms to a fluorite structure when the Frenkel pair to cation ratio reaches 0.2 and that subsequent irradiation introduces more Frenkel pairs that are sufficient to drive the amorphisation process. They also state that the necessity to reach this critical concentration of Frenekl pair defects is the reason that $La_2Zr_2O_7$ is so difficult to amorphise at room temperature as, at this temperature, the cations have sufficient mobility to move back from the interstitial sites to equivalent lattice sites [266].

5.3 Methodology

5.3.1 Interatomic Potentials

The full charge interatomic potentials from Minervini *et al.* [223] and Stanek *et al.* [230] were used to model the pyrochlore compounds and the U^{4+} potential from Busker *et al.* [267] was used to simulate UO_2. Potential parameters for U^{3+}, Pu^{3+} and Pu^{4+} were derived for this study. Since no structural data for compounds containing U^{3+} ions could be found, rendering the multi fitting procedure described in chapter 3 impossible, this potential was derived differently using a method similar to that used by Butler *et al.* [268]. In this procedure, the interatomic interactions were plotted for the Pu^{3+} and the

Pu^{4+} and the difference between the two was calculated. The U^{4+} potential was plotted and then the difference between the Pu^{3+} and the Pu^{4+} was subtracted. A line of best fit taking the mathematical form of the Buckingham potential was fit to this new curve (see equation 3.7) and the A, ρ and C parameters thereby identified. All potentials used are shown in Table 5.1. The shell model was used for the oxygen, zirconium and lead ions and these parameters are reported in table 5.2

Special attention has been paid to the derivation of a new Pu^{3+}-O^{2-} short-range potential. The parameters were selected to best fit the lattice parameters of Pu_2O_3, $CrPuO_3$ and $AlPuO_3$ while exactly reproducing the lattice parameter of stoichiometric $Pu_2Zr_2O_7$ reported in reference [240] (i.e. 10.70Å). In previous computational work [234] potentials were fitted to a lattice parameter corresponding to a hyper-stoichiometric $Pu_2Zr_2O_7$ material i.e. containing Pu^{4+} [240, 242].

The energy minimisation atomic scale simulation approach described (see chapter 3) has been used successfully to predict various properties of $A_2B_2O_7$ pyrochlores, including oxygen migration [221], intrinsic disorder process energies [223] and nonstoichiometry formation via solution of excess BO_2 or A_2O_3 [220]. One approximation that should be mentioned is that all pyrochlores are treated as cubic. While this is the case for the majority of pyrochlore compositions, there are a few titanates with large lanthanide cations and $Pu_2Ti_2O_7$ which exhibit a monoclinic distortion [135, 223] (see also chapter 4).

Table 5.1: Full charge short range potential parameters used to describe interactions between all the ions in this study.

Species	A (eV)	ρ (eV)	C (eV Å^6)
$O^{2-} \leftrightarrow O^{2-}$	9547.960	0.21920	32.00
$La^{3+} \leftrightarrow O^{2-}$	2088.890	0.34600	23.25
$Pr^{3+} \leftrightarrow O^{2-}$	2055.350	0.34380	23.95
$Nd^{3+} \leftrightarrow O^{2-}$	1995.200	0.34300	22.59
$Sm^{3+} \leftrightarrow O^{2-}$	1944.440	0.34140	21.49
$Eu^{3+} \leftrightarrow O^{2-}$	1925.710	0.34030	20.59
$Gd^{3+} \leftrightarrow O^{2-}$	1885.750	0.33990	20.34
$Dy^{3+} \leftrightarrow O2-$	1807.840	0.33930	18.77
$Er^{3+} \leftrightarrow O^{2-}$	1739.910	0.33890	17.55
$Yb^{3+} \leftrightarrow O^{2-}$	1649.800	0.33860	16.57
$Lu^{3+} \leftrightarrow O^{2-}$	1618.800	0.33849	19.27
$U^{3+} \leftrightarrow O^{2-}$	1165.65	0.376582	0.00
$Pu^{3+} \leftrightarrow O^{2-}$	1150.745	0.37430	12.10
$Ti^{4+} \leftrightarrow O^{2-}$	2131.040	0.30380	0.00
$Ru^{4+} \leftrightarrow O^{2-}$	1215.780	0.34410	0.00
$Mo^{4+} \leftrightarrow O^{2-}$	1223.970	0.34700	0.00
$Sn^{4+} \leftrightarrow O^{2-}$	1414.320	0.34790	13.66
$Zr^{4+} \leftrightarrow O^{2-}$	1502.110	0.34770	5.10
$Pb^{4+} \leftrightarrow O^{2-}$	1640.340	0.35070	19.50
$U^{4+} \leftrightarrow O^{2-}$	1761.775	0.356421	0.00
$Pu^{4+} \leftrightarrow O^{2-}$	1762.840	0.35420	11.48

Table 5.2: Shell parameters used to describe interactions between all the ions with shells in this study.

Species	Charge	k
O^{2-}	-2.04	32.0
Zr^{4+}	-0.05	189.7
Pb^{4+}	-0.05	205.0

5.3.2 Contour Maps

All results are presented in the form of host lattice composition contour maps (see figures 5.1 to 5.12). These show the results as a two dimensional surface where the x-axis represents increasing B cation radius and the y-axis represents increasing A cation radius. Isolines link compositions of equal energy and the shade of the areas bounded by these lines indicates an energy interval as shown in the separate scale. On the energy surface, actual calculations (i.e. experimentally observed pyrochlore forming compositions, see figure 4.19 in chapter 4) are marked by points whose shape represents the solution mechanism from which the energy for that composition is taken.

5.4 Results and Discussion

5.4.1 Solution Mechanisms

As in previous work by Weber *et al.* [234] solution is considered with respect to the binary oxides MeO_2 and Me_2O_3 where Me is either U or Pu (although experimental data for U_2O_3 could not be located, here it is as-

sumed to form isostructurally with Pu_2O_3). Since these simple oxides have a different stoichiometry to a host pyrochlore it will be necessary to form charge compensating defects. Solution process energies are then composed of a number of individual defect energies. Possible solution processes are described by equations 5.1 to 5.14 using Kröger-Vink notation [5]. Solution processes which involve cation interstitial ions will not be reported as it was found that the corresponding solution energies are highly unfavourable, similar results were reported by Williford and Weber [234].

Equations 5.1 through 5.3 describe the solution of Me_2O_3 into $A_2B_2O_7$ pyrochlore with compensation by oxygen vacancies $\left(V_O^{\bullet\bullet}\right)$. These mechanisms maintain the pyrochlore A:B ratio but not the pyrochlore oxygen stoichiometry. Equation 5.1 assumes the actinide exclusively occupies the A sites in the pyrochlore. Equation 5.2 assumes equal A and B site occupation of the actinide ions and equation 5.3 assumes only B site occupation (note that equation 5.2 is related to equations 5.1 and 5.3 through antisite disorder). Equation 5.4 assumes that the actinide ion exclusively occupies the A site but allows the formation of excess A_2O_3 (i.e. we introduce Me_2O_3 into the lattice and remove A_2O_3) and consequently the A:B ratio is no longer maintained but the oxygen stoichiometry is unaltered (this is the same as equation 1 in [234]). Equation 5.5 assumes that the actinide ion occupies the B site, but results in the formation of excess BO_2. Consequently neither the A:B ratio nor the oxygen stoichiometry are maintained (this is the same as equation 2 in [234]).

$$2\mathrm{Me_2O_3} + 4A_A^{\times} + 2B_B^{\times} + \mathrm{O}_O^{\times} \longrightarrow 4\mathrm{Me}_A^{\times} + 2A_B^{\prime} + V_O^{\bullet\bullet} + A_2B_2\mathrm{O_7} \qquad (5.1)$$

$$2\mathrm{Me_2O_3} + 2A_A^{\times} + 2B_B^{\times} + \mathrm{O}_O^{\times} \longrightarrow 2\mathrm{Me}_A^{\times} + 2\mathrm{Me}_B^{'} + V_O^{\bullet\bullet} + A_2B_2\mathrm{O_7} \quad (5.2)$$

$$2\mathrm{Me_2O_3} + 2A_A^{\times} + 4B_B^{\times} + \mathrm{O}_O^{\times} \longrightarrow 2B_A^{\bullet} + 4\mathrm{Me}_B^{'} + V_O^{\bullet\bullet} + A_2B_2\mathrm{O_7} \quad (5.3)$$

$$\mathrm{Me_2O_3} + 2A_A^{\times} \longrightarrow 2\mathrm{Me}_A^{\times} + A_2\mathrm{O_3} \quad (5.4)$$

$$\mathrm{Me_2O_3} + 2B_B^{\times} + \mathrm{O}_O^{\times} \longrightarrow 2\mathrm{Me}_B^{'} + V_O^{\bullet\bullet} + 2B\mathrm{O_2} \quad (5.5)$$

Equations 5.6 through 5.8 describe the solution of PuO_2 and UO_2 (i.e. MeO_2) with compensation via oxygen interstitial ions $\big($i.e. $\mathrm{O}_i^{''}$ where in all cases the interstitial site is the unoccupied 8a lattice position of the $Fd\overline{3}m$ space group$\big)$. Equation 5.6 assumes the actinide exclusively occupies the A sites in the pyrochlore. Equation 5.7 assumes equal A and B site occupation of the actinide ions and equation 5.8 assumes B site occupation. Equation 5.9 assumes that the actinide ion exclusively occupies the A site but allows the formation of excess A_2O_3 (equation 4 in [234]) and Equation 5.10 assumes that the actinide ion occupies the B site, allowing the formation of excess BO_2 (this is equation 3 in [234]).

$$4\mathrm{MeO_2} + 4A_A^{\times} + 2B_B^{\times} \longrightarrow 4\mathrm{Me}_A^{\bullet} + 2A_B^{'} + \mathrm{O}_i^{''} + A_2B_2\mathrm{O_7} \quad (5.6)$$

$$4\mathrm{MeO_2} + 2A_A^{\times} + 2B_B^{\times} \longrightarrow 2\mathrm{Me}_A^{\bullet} + 2\mathrm{Me}_B^{\times} + \mathrm{O}_i^{''} + A_2B_2\mathrm{O_7} \quad (5.7)$$

$$4\mathrm{MeO_2} + 2A_A^{\times} + 4B_B^{\times} \longrightarrow 2B_A^{\bullet} + 4\mathrm{Me}_B^{\times} + \mathrm{O}_i^{''} + A_2B_2\mathrm{O_7} \quad (5.8)$$

$$2\mathrm{MeO_2} + 2A_A^{\times} \longrightarrow 2\mathrm{Me}_A^{\bullet} + \mathrm{O}_i^{''} + A_2\mathrm{O_3} \quad (5.9)$$

$$\mathrm{MeO_2} + B_B^{\times} \longrightarrow \mathrm{Me}_B^{\times} + B\mathrm{O_2} \quad (5.10)$$

Equations 5.11 through 5.14 describe the solution of MeO_2 via the formation of charge compensating A cation vacancies $\left(V_A^{'''}\right)$. Equations 5.11 through 5.13 are equivalent to 5.6 through 5.8. As such these mechanisms maintain the A:B ratio of the pyrochlore. Equation 5.14 is equivalent to equation 5.9 (this is equation 5 in [234]).

$$7\mathrm{MeO_2} + 8A_A^{\times} + 4B_B^{\times} \longrightarrow 7\mathrm{Me}_A^{\bullet} + V_A^{'''} + 4A_B^{'} + 2A_2B_2\mathrm{O_7} \tag{5.11}$$

$$7\mathrm{MeO_2} + 4A_A^{\times} + 4B_B^{\times} \longrightarrow 3\mathrm{Me}_A^{\bullet} + 4\mathrm{Me}_B^{\times} + V_A^{'''} + 2A_2B_2\mathrm{O_7} \tag{5.12}$$

$$7\mathrm{MeO_2} + 4A_A^{\times} + 7B_B^{\times} \longrightarrow 7\mathrm{Me}_B^{\times} + 3B_A^{\bullet} + V_A^{'''} + 2A_2B_2\mathrm{O_7} \tag{5.13}$$

$$3\mathrm{MeO_2} + 4A_A^{\times} \longrightarrow 3\mathrm{Me}_A^{\bullet} + V_A^{'''} + 2A_2\mathrm{O_3} \tag{5.14}$$

Next solution mechanisms that involve co-doping were considered (such mechanisms were not considered in [234]). Equation 5.15 describes solution of trivalent Pu^{3+} or U^{3+} accompanied by additional B^{4+} ions. Equation 5.16 assumes tetravalent PuO_2 or UO_2 and additional A^{3+} ions.

$$\mathrm{Me_2O_3} + 2BO_2 + 2A_A^{\times} + 2B_B^{\times} \longrightarrow 2\mathrm{Me}_A^{\times} + 2B_B^{\times} + A_2B_2\mathrm{O_7} \tag{5.15}$$

$$2\mathrm{MeO_2} + A_2\mathrm{O_3} + 2A_A^{\times} + 2B_B^{\times} \longrightarrow 2A_A^{\times} + 2\mathrm{Me}_B^{\times} + A_2B_2\mathrm{O_7} \tag{5.16}$$

$$2\mathrm{Pu}_A^{\times} + A_2B_2\mathrm{O_7} \longrightarrow 2A_A^{\times} + \mathrm{Pu_2}B_2\mathrm{O_7} \tag{5.17}$$

$$\mathrm{CaBO_3} + \mathrm{MeO_2} + BO_2 + 2A_A^{\times} \longrightarrow \mathrm{Ca}_A^{'} + \mathrm{Me}_A^{\bullet} + A_2B_2O_7 \tag{5.18}$$

Equation 5.15 results in a solid solution of $Me_2B_2O_7$ and $A_2B_2O_7$. The

stability of this solid solution is investigated through equation 5.17 which allows the solid solution to decompose into the two component pyrochlores. This is equivalent to the process investigated by Shoup *et al.* (1996) for Pu.

Equation 5.16 results in a composition that can be considered a solid solution between $A_2Me_2O_7$ and $A_2B_2O_7$, except that no $A_2Me_2O_7$ pyrochlores have been observed. However, on the basis of these atomistic simulations it is found that $La_2Pu_2O_7$ and $Pr_2Pu_2O_7$ are stable with respect to PuO_2 and A_2O_3 and that $La_2U_2O_7$ is stable with respect to La_2O_3 and UO_2. Of course, Pu^{4+} is only stable at higher oxygen pressures, in which case it is possible that Pr (but not La) will also attain a tetravalent charge state, resulting in a fluorite solid solution. The predicted lattice parameter of stoichiometric $La_2Pu_2O_7$ is 11.14 Å, that of $Pr_2Pu_2O_7$ is 11.05 Å and $La_2U_2O_7$ is 11.23 Å. Predicted lattice parameters and formation energies of other actinide containing pyrochlores are mentioned later in section 5.4.2.

The final solution mechanism, equation 5.18, also concerns the co-solution of tetravalent uranium or plutonium onto trivalent A pyrochlore sites. This solution is charge compensated by Ca^{2+}, also on A sites. The mechanism is the dilute limit equivalent of the pyrochlore formation mechanism investigated by Huifang *et al.* [37]. The calcium is assumed to be provided in the form of a perovskite; $CaBO_3$ (see equation 5.18).

The sum of the individual defect energies and formation energies from equations 5.1 through 5.16 cannot be directly compared until they have been normalised. This process and its rationale is described in reference [5] and an example is given in appendix B. The normalisation factors for equations

5.1 through 5.16 are simply equal to the number of defect species on the right hand side of the equation. For example, with mechanism 5.1 the factor is 7 and for mechanism 5.2 it is 5. Only normalised energies will be presented in the subsequent sections.

5.4.2 Formation of Actinide Pyrochlores

Finally reactions that describe the formation of Pu^{3+} and U^{3+} actinide pyrochlores are also considered (equations 5.19 and 5.20).

$$Me_2O_3 + 2BO_2 \longrightarrow Me_2B_2O_7 \tag{5.19}$$

$$A_2O_3 + 2MeO_2 \longrightarrow A_2Me_2O_7 \tag{5.20}$$

The predicted lattice parameters and formation energies are given in table 5.3 which shows that all $U_2B_2O_7$ and $Pu_2B_2O_7$ pyrochlores are stable with respect to the basic oxides. The lattice parameters for the three $A_2Me_2O_7$ pyrochlores mentioned in the solution mechanisms section are also given. While the hypothetical $U_2B_2O_7$ pyrochlores are not predicted to be as stable as their Pu counterparts they are all predicted to form from mixtures of U_2O_3 and BO_2. They are considered hypothetical, however, as U_2O_3 has not been found to form experimentally and therefore $U_2B_2O_7$ will not be stable with respect to oxidation to a $U_2B_2O_8$ or $(U,B)O_2$ fluorite solid solution. Similarly as found by Kulkarni *et al.* [242] it is likely that the Pu^{3+} containing materials will easily oxidise to form fluorite solid solutions rather than pyrochlores.

Table 5.3: Predicted formation energy and lattice parameter for simulated actinide pyrochlores.

Compound	Lattice Parameter (Å)	Formation Energy (eV)
$U_2Ti_2O_7$	10.305	-1.10
$U_2Ru_2O_7$	10.413	-1.60
$U_2Mo_2O_7$	10.482	-1.68
$U_2Sn_2O_7$	10.639	-1.61
$U_2Zr_2O_7$	10.777	-1.49
$U_2Pb_2O_7$	10.914	-1.06
$La_2U_2O_7$	11.233	-0.76
$Pr_2U_2O_7$	N/A	0.34
$Pu_2Ti_2O_7$	10.228	-2.23
$Pu_2Ru_2O_7$	10.332	-2.61
$Pu_2Mo_2O_7$	10.402	-2.62
$Pu_2Sn_2O_7$	10.560	-2.40
$Pu_2Zr_2O_7$	10.700	-2.16
$Pu_2Pb_2O_7$	10.837	-1.62
$La_2Pu_2O_7$	11.139	-1.19
$Pr_2Pu_2O_7$	11.048	-0.14
$Nd_2Pu_2O_7$	N/A	0.12
$Sm_2Pu_2O_7$	N/A	0.47

5.4.3 Solution Results

Symbols used on Contour Maps

On the following contour maps:

- Diamond shaped points represent mechanism 5.4.
- Square shaped points represent mechanism 5.6.
- Circular shaped points represent mechanism 5.7.
- Triangle shaped points represent mechanism 5.10.
- Star shaped points are used for co-solution or co-doping mechanisms where only one reaction was considered per plot including mechanisms 5.15, 5.16 and 5.18. The mechanism will be specified in the figure caption.
- Pentagon shaped points represent mechanism 5.17.

5.4.4 Solution of Pu_2O_3 and U_2O_3 into Pyrochlores

Initially the approach of Williford and Weber [234] was followed and the solution of the binary oxide Pu_2O_3 via a number of mechanisms (equations 5.1-5.5) was compared. However, given the observations in $Gd_2Zr_2O_7$ by the previous authors [234] interstitial compensation mechanisms were not taken into account but a greatly extended set of oxygen vacancy compensation mechanisms was considered. This selection of solution mechanisms is further

justified by the work on A_2O_3 excess non-stoichiometry [220] which showed that interstitial mechanisms were considerably less favourable compared to oxygen vacancy compensation over the whole compositional range.

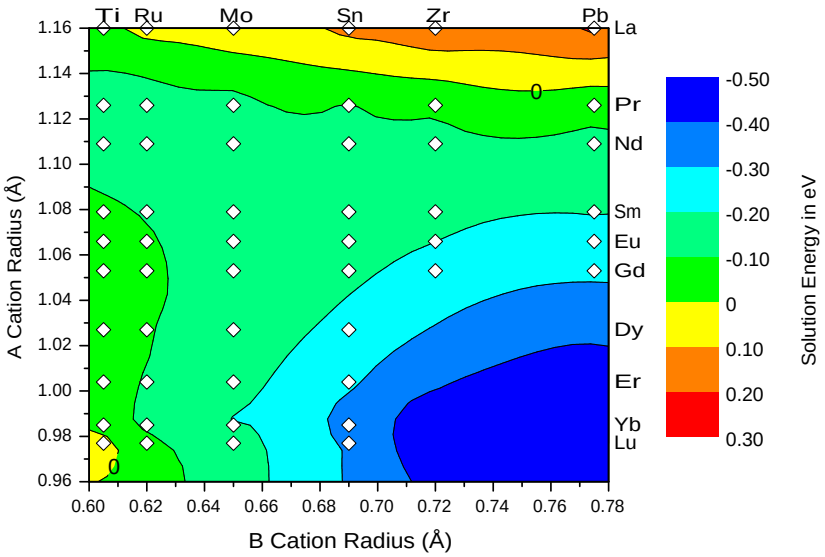

Figure 5.1: Solution of Pu_2O_3 (eV) into pyrochlores. All actual compositions are indicated by points on the map. Diamond shaped points indicate mechanism 5.4.

Results for the solution of Pu_2O_3 are presented in figure 5.1. For each composition the energy selected for the map corresponds to the lowest energy solution mechanism (this will also be the case in subsequent maps). Since at each composition the shape of the point is a white diamond, this indicates that the lowest energy mechanism was independent of composition and corresponds to equation 5.4. Thus, not only is the same lowest solution mechanism in $Gd_2Zr_2O_7$ as Williford and Weber [234] reported but this observation holds true for all the pyrochlores. Consequently, the solution of Pu_2O_3 always results in Pu^{3+} ions exclusively occupying the A sites.

As with the previous work [234], a negative solution energy for Pu_2O_3 in $Gd_2Zr_2O_7$ is also found and this value is -0.23eV. As compositions approach those pyrochlores with either: (1) larger A cations; or (2) small lattice parameters (this includes many of the titanates); solution energies approach zero and become positive. Such compositions may therefore be less useful for fabricating materials under reducing conditions.

This observed lowest energy solution mechanism is a consequence of the Pu^{3+} ion substituting for an isovalent A site ion with a radius of 1.00Å which places it toward the low end of A cation radii for pyrochlores. Thus there is never much lattice relaxation associated with this substitutional defect and consequently the energy for this process is lower than the energies for equations the process in 5.2, 5.3 and 5.5 which have Pu^{3+} ions substituting onto the smaller B^{4+} sites. Equation 5.4 is more favourable than equation 5.1 because the energy to form A_2O_3 is lower than that for the formation of an A cation anti-site defect and $A_2B_2O_7$. Nevertheless equation 5.1 is the next most favourable but it is always more than 0.58eV less favourable than equation 5.4.

Results for the solution of U_2O_3 into pyrochlores are now presented in figure 5.2. At first glance is appears very similar to that for the solution of Pu_2O_3 as the contour shapes are similar and again solution across the entire range is dominated by isovalent substitution of U^{3+} onto the A site (as in equation 5.4). It should be noted that while most solution energies for Pu^{3+} were negative, those for U^{3+} are mostly positive with the solution energies on average 0.3 eV higher than for the equivalent Pu^{3+} solution. This means

that only $Yb_2Sn_2O_7$ and $Lu_2Sn_2O_7$ show negative solution energies although $Gd_2Zr_2O_7$ is very close to zero at 0.017 eV.

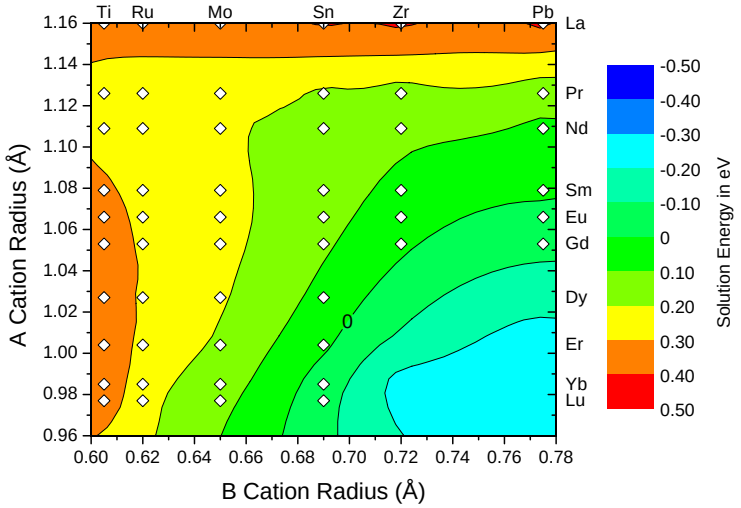

Figure 5.2: Solution of U_2O_3 (eV) into pyrochlores. All actual compositions are indicated by points on the map. Diamond shaped points indicate mechanism 5.4.

Alternative co-solution mechanisms for Pu_2O_3 with BO_2 (i.e. equation 5.15) are now examined and the results are shown in Figure 5.3. This mechanism represents a possible fabrication process. It is immediately apparent that co-solution energies are significantly more negative than for simple Pu_2O_3 solution and also shows a stronger compositional variation (i.e. more contours). However, although the resulting compositions $A_{2-x}Pu_xB_2O_7$ may be stable with respect to the simple starting oxides, the equation hides the possibility that decomposition to a mixture of $A_2B_2O_7$ and $Pu_2B_2O_7$ may occur. This is investigated in Figure 5.4 where negative energies imply that decomposition is just favourable for pyrochlores with A cation radii smaller than Nd. However, the predicted internal energies for such a de-mixing are very

small, never larger than 0.13eV per $Pu_2B_2O_7$. Certainly the configurational entropy of mixing of two pyrochlores (a term not included in these calculations) would ensure that the solid solutions remain mixed; furthermore cation migration activation energies are known to be high in pyrochlores [269]. Consequently, under reducing conditions where Pu^{3+} remains stable with respect to Pu^{4+}, significant solid solubility of $Pu_2B_2O_7$ in $A_2B_2O_7$ is expected (unless there is an excess of A_2O_3 in which case the results presented in Figure 5.1 have significance). This is supported by the experimental data of Shoup *et al.* [36] in that they observed extensive solid solubility of $Pu_2Ti_2O_7$ in $Ln_2Ti_2O_7$. However, contrary to the present predictions which would suggest increasing solubility with increasing A host cation radius (as the host cation approaches the Pu^{3+} radius), Shoup *et al.* [36] observed a decreasing solubility with increasing A cation radius.

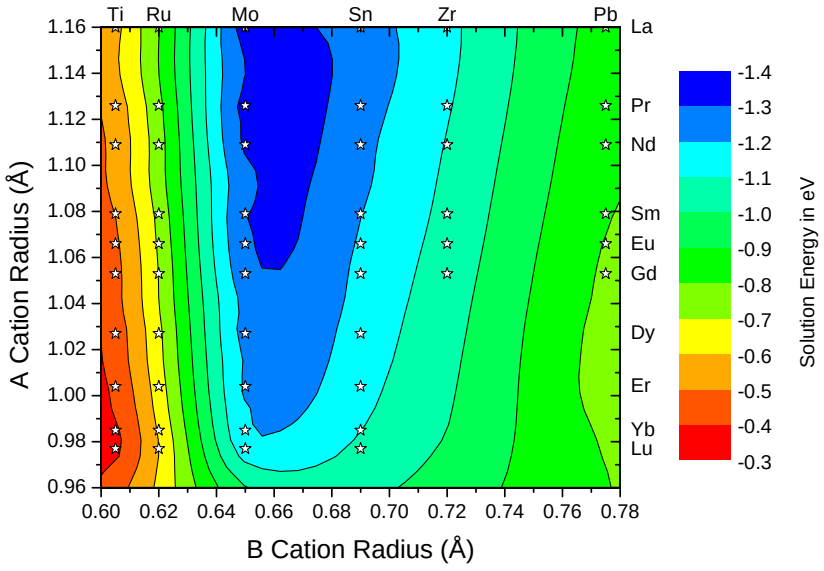

Figure 5.3: Energies of Pu_2O_3 and BO_2 co-solution in pyrochlores via mechanism 5.15.

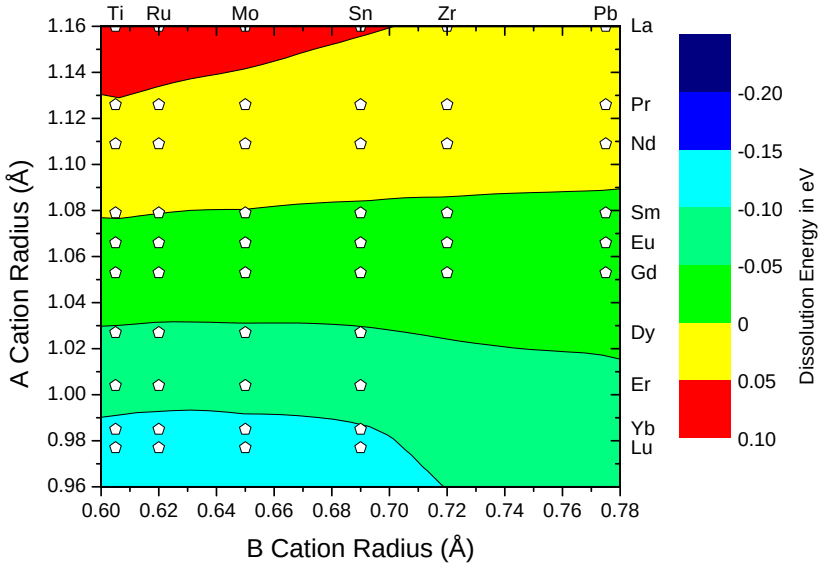

Figure 5.4: Energy to dissociate $A_{2-x}Pu_xB_2O_7$ into $A_2B_2O_7$ and $Pu_2B_2O_7$ via mechanism 5.17.

The results for the equivalent U^{3+} co-solution are presented in figure 5.5. As can be seen by comparing this with figure 5.3, there are both similarities and differences. The same trends are noted in that all the values are negative indicative that this process is favourable for all pyrochlore compositions unlike the simple solution method described by equation 5.4 and shown in figure 5.2. Another similar trend is that the solution energies are at a minimum for the molybdate pyrochlores but the depth of this minimum is no where near as great, being about 0.5 eV higher that for the Pu doped material. As with Pu^{3+} solution, decomposition to form a mixture of $A_2B_2O_7$ and $U_2B_2O_7$ was considered. It is found that this process is more favourable than for Pu^{3+}, this is most likely due to the slightly larger cation radius of U^{3+} (1.025 Å [174]), placing it in the mid range of stable pyrochlore forming compounds. The decomposition energy for this process reaches a maximum of about 0.2 eV which may be significant enough to allow this to proceed if conditions ever become reducing enough to form U^{3+}.

As an alternative to co-solution, the possibility that defect clusters might form as a result of solution via equations 5.1, 5.2 and 5.3, through the association of oppositely charged defects [223,267] was also considered. Although the clusters were stable with respect to the isolated defects, this did not cause any solution mechanisms to be as stable as either equation 5.4 or 5.15 (in which defects are charge neutral and thus have negligible binding energies).

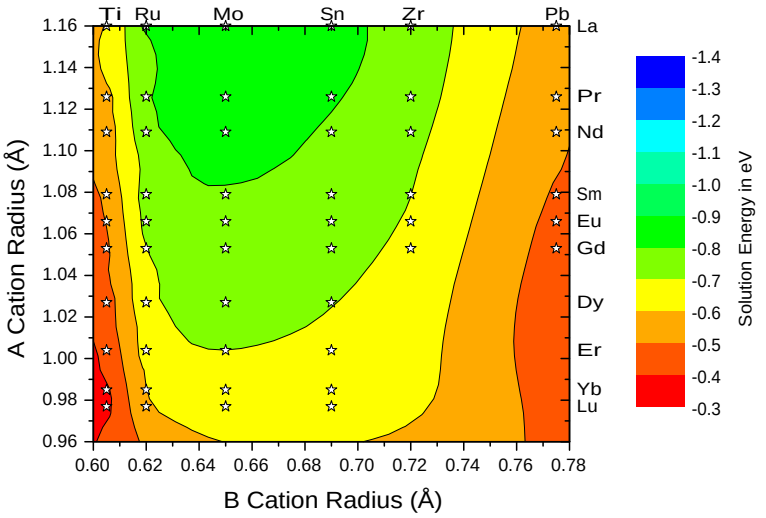

Figure 5.5: Energies of U_2O_3 and BO_2 co-solution in pyrochlores via mechanism 5.15

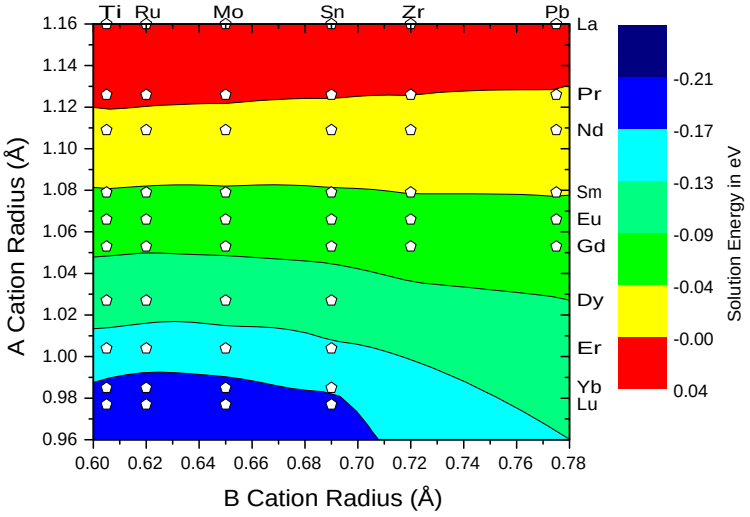

Figure 5.6: Energy to dissociate $A_{2-x}U_xB_2O_7$ into $A_2B_2O_7$ and $U_2B_2O_7$ via mechanism 5.17

5.4.5 Solution of PuO_2 and UO_2

Results for Pu^{4+} solution from PuO_2 are presented in figure 5.7. By examining the $Gd_2Zr_2O_7$ composition first, it can be seen that the figure shows a white circle and thus equation 5.7 is the lowest energy solution mechanism at this composition and Pu^{4+} will occupy both A and B cation sites. This is different to the prediction of Williford and Weber [234] who favoured equation 5.10 in which Pu^{4+} occupies only B cation sites. However, these authors did not consider equation 5.7 although the difference between equations 5.7 and 5.10 at this composition is only 0.17 eV. If the calculations for equations 5.7 and 5.10 are repeated using the potentials of Williford and Weber [234], it is found that the difference between the equations is reduced to only 0.05eV, but equation 5.7 remains energetically more favourable. In all cases energies are positive indicating a significant limit to the solubility of PuO_2 in $Gd_2Zr_2O_7$ this type of process.

Now the solution of PuO_2 is considered over the broad range of pyrochlore compositions. For the most stable pyrochlore forming materials (i.e. away from the large B cation, small A cation region, see [223]) figure 5.7 shows that equation 5.10 does now become more favourable than equation 5.7. Finally for stannates with small A cations equation 5.6 is preferred so that Pu^{4+} substitutes exclusively on the A cation site. However, the difference between equations 5.6 and 5.7 is never greater than 0.06 eV.

Despite the availability of different solution mechanisms, solution energies remain positive. As such, the solution of PuO_2 is clearly less favourable compared to the solution of Pu_2O_3.

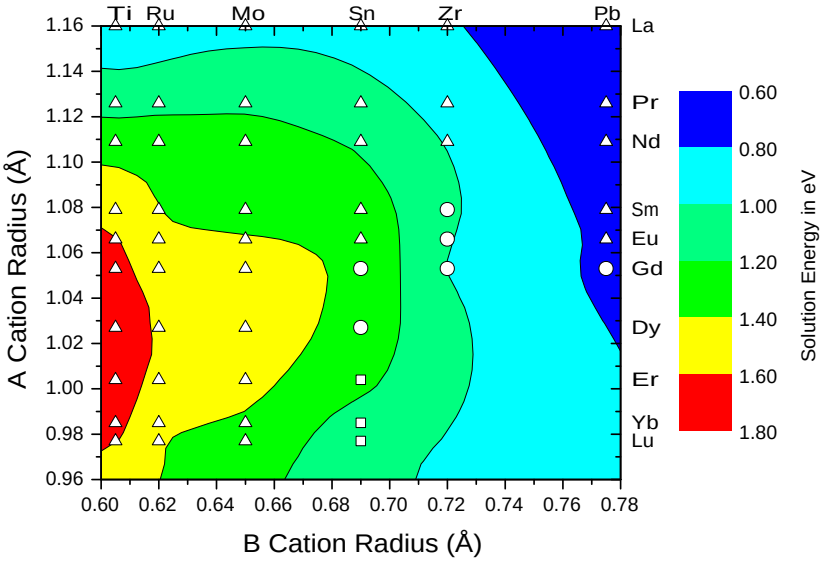

Figure 5.7: Energies of solution of PuO_2 into pyrochlores. The triangle shaped points show where mechanism 5.10 is most favourable, white circles correspond to mechanism 5.7 and white squares to mechanism 5.6.

Differences in preferred solution mechanism have been noted previously between the more stable pyrochlore forming compositions and compositions approaching the pyrochlore to fluorite boundary [220]. With this in mind, the reason why $Gd_2Zr_2O_7$ pyrochlore (which is close to fluorite forming compositions) shows a preference for equation 5.7 is that it incorporates oxygen interstitial ions, O_i''. These charge compensating defects occupy the 8a Wyckoff site which is occupied in fluorite but not in pyrochlore. Away from the pyrochlore fluorite boundary greater distortions of the lattice around the 8a site make it less favourable to accommodate an oxygen interstitial ion.

Figure 5.8 shows the calculated energies for the solution of UO_2. These values are very similar to those for Pu^{4+}, however, there are marked differences in

preferred solution mechanisms. In particular, there is a broad compositional region between equations 5.6 or 5.7 and 5.10 where the preferred mechanism is equation 5.11. In this case the charge compensating defect is an A cation vacancy. This type of mechanism was previously identified as important in the study of BO_2 excess nonstoichiometry in pyrochlores [220]; consequently it is not surprising to find it is important here. If the energies for equations 5.11 and 5.10 are compared in this compositional region, the difference is always less than 0.30 eV. Furthermore, the differences between equations 5.11 and 5.7 are always less than 0.15 eV (for the same compositional region). What therefore emerges is the possibility of a complex equilibrium between equations 5.6, 5.7, 5.10 and 5.11 with only a small difference between the three energies of solution at a given position within this extended compositional range. Nevertheless, there are differences in the overall solution energy for UO_2 between compositions and it is expected that this reflects a real variation in the extent of UO_2 solution (throughout differences rather than absolute values are emphasised).

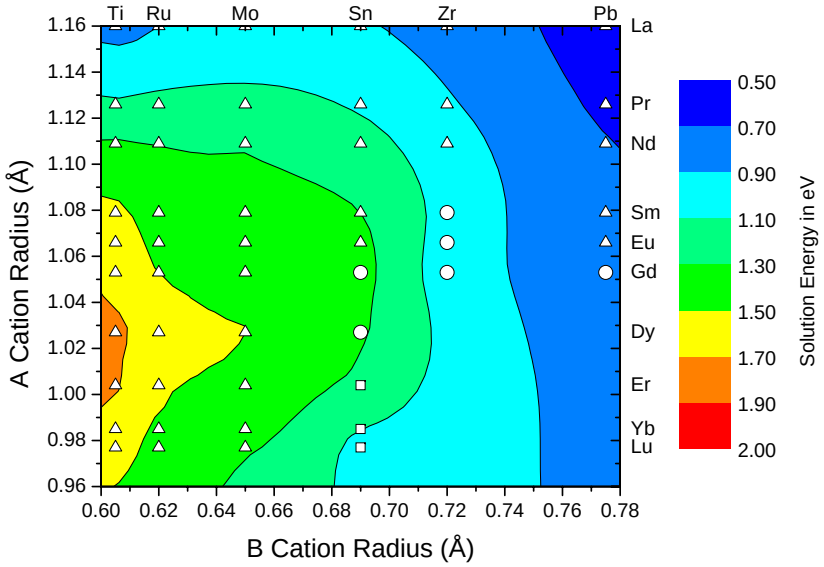

Figure 5.8: Solution energies for UO_2 into pyrochlores. The triangle shaped points show where mechanism 5.10 is the most favoured, white circles to mechanism 5.7 and white squares to mechanism 5.6.

Finally, the co-solution of PuO_2 and A_2O_3 is considered as a mechanism for overcoming the positive solution energies for Pu^{4+} described in figure 5.7. This results in a material with a composition $A_2\,(B_{1-x}Pu_x)O_7$. If the PuO_2 and Gd_2O_3 co-solution is considered first, the result which is presented in figure 5.9, shows that co-solution only lowers the solution energy from 0.98 eV (via equation 5.7) to 0.46 eV (equation 5.16). Nevertheless, clearly solution is still not favourable. However, if the broader compositional range is considered, solution is predicted to be favourable for materials with large A cations, independently of the B cation radius. This is a considerable improvement over solution of PuO_2 alone but only in this upper half of the compositional range (compare to figure 5.7). By comparing figures 5.7 and 5.9 it is also clear that the compositional variation in co-solution energies is

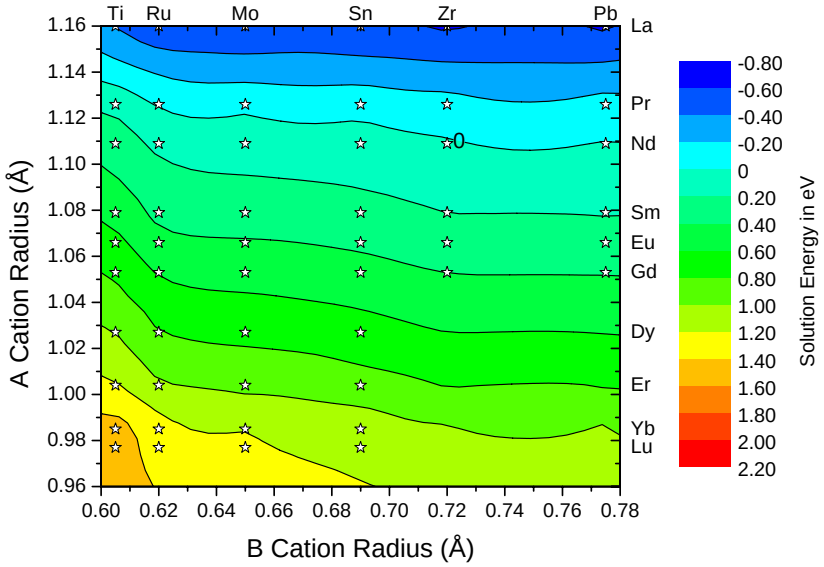

Figure 5.9: Co-solution energies for PuO_2 and A_2O_3 into pyrochlores via mechanism 5.16.

greater than for the simple solution mechanisms.

Results for co-solution of UO_2 show essentially the same trends in solution energies as a function of A and B host cation size (see figure 5.10). However, as with simple solution mechanisms, UO_2 co-solution is consistently less favourable than PuO_2 co-solution (by between 0.2-0.4 eV)

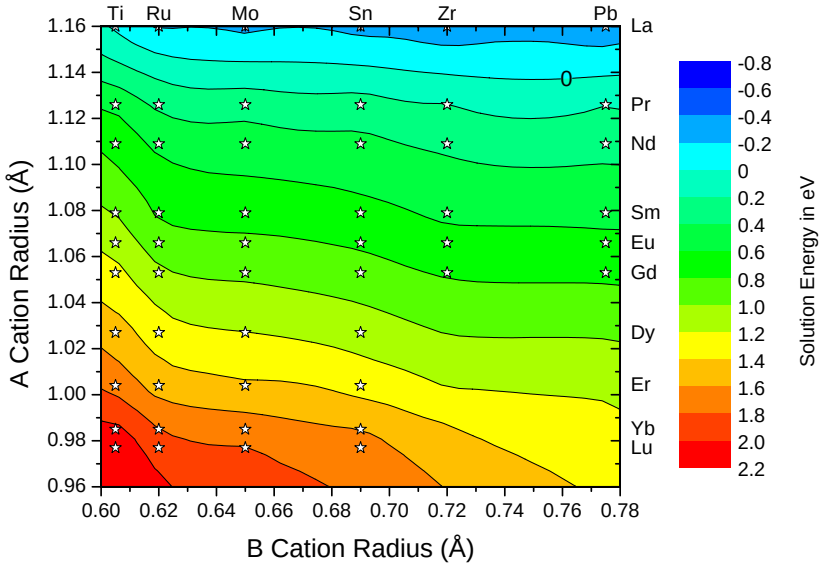

Figure 5.10: co-solution energies for UO_2 and A_2O_3 in pyrochlores via mechanism 5.16.

5.4.6 Solution of PuO_2/UO_2 with compensation via Ca^{2+}

The results of the Ca^{2+} mediated co-solution mechanism (equation 5.18) are presented for Pu^{4+} in figure 5.11. The essential feature of this figure is the generally small compositional variation in solution energy, especially with respect to A cation radius. This is surprising since both Ca^{2+} and Pu^{4+} substitute onto the A site, however, their A site energy variation when combined with the compositional variation in $A_2B_2O_7$ lattice energy, effectively cancel to yield little A site dependence. The small positive solution energies also indicate that the plutonium solution limit may be low and an associated zirconolite or betafite like phase may form. Ideally a phase equilibria investigation is now required to further the study of actinide accommodation.

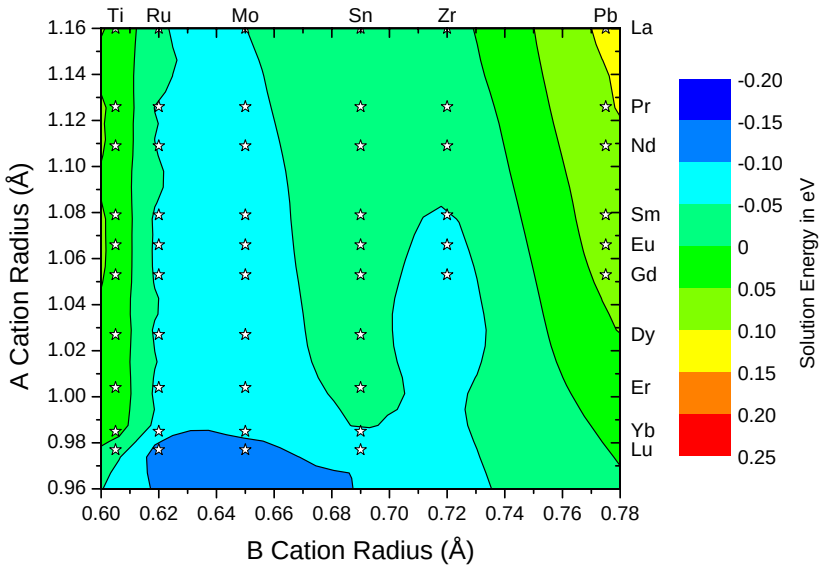

Figure 5.11: co-solution energies for PuO_2 and $CaBO_3$ into pyrochlores via mechanism 5.18.

If figures 5.11 and 5.9 are compared (noting the scale differences), it is at once apparent that equation 5.18 provides a much lower solution energy for compositions with smaller A cations (below Nd) but not for larger A cations (above Nd). Equivalent results are seen for U^{4+} by comparing figures 5.10 and 5.12. Indeed solutions of Pu^{4+} and U^{4+} via equation 5.18 have generally similar energies. An exception to this is in the titanate pyrochlores (comparing figures 5.11 and 5.12) where it seems U^{4+} solution is rather less favourable than Pu^{4+}. This may have a bearing on the observations of [30] who observed Pu^{4+} in calcium titanate pyrochlores and U^{5+} rather than U^{4+}.

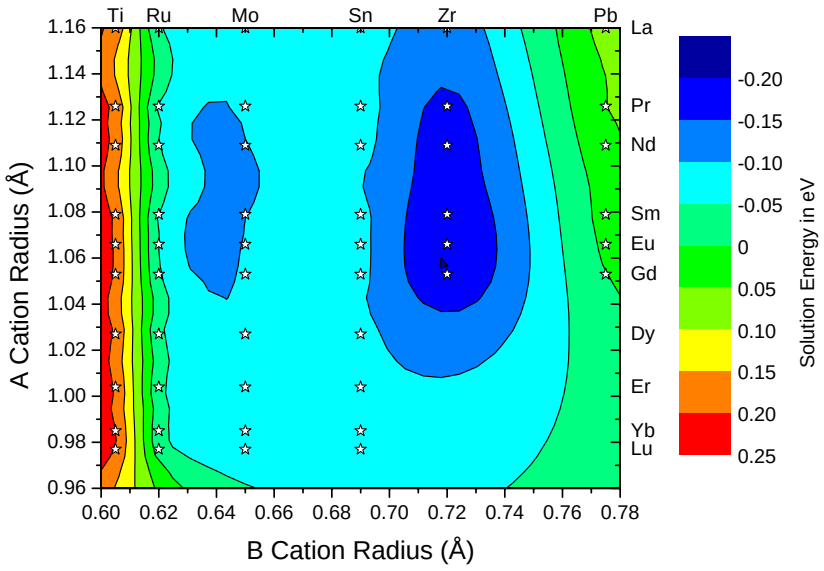

Figure 5.12: Co-solution energies of UO_2 and $CaBO_3$ into pyrochlores via mechanism 5.18.

5.5 Summary

The aim of this study is to provide predictions for how solution mechanisms and energies of trivalent Pu^{3+} and U^{3+} and tetravalent Pu^{4+} and U^{4+} might vary as a function of composition in pyrochlore oxides. Solution of simple sesquioxides and dioxides has been considered and extended to consider co-solution mechanisms, although all types are likely to be of interest given the complexity of processes that occur during fabrication of nuclear materials and in their subsequent aging. Waste form solution chemistry is indeed rich and varied. Consequently, it is not intended to imply that even a majority of the possible processes that might occur in these systems have been investigated. However, it is hoped that the results might provide a direction or framework on which further studies can be based. For example, since computational resources continue to grow apace, it will become typical to extract free energies of solution from such atomistically based complex reactions [270]. Furthermore it will be possible to routinely calculate these energies using quantum mechanical techniques. For more simple systems and single compositions this is already the case [224]. In the meantime discussions can be based on relative energies calculated more approximately, as here.

In the results section variations across compositions were discussed in detail. For example, the simulations are consistent with the solution of Pu^{3+} from Pu_2O_3 proceeding via a single mechanism independent of composition (see figure 5.1) while the solution mechanism for Pu^{4+} varies greatly as a function of composition (see figure 5.7). A comparison between ions can also be made so that the relative solution of plutonium charge states can be considered,

as can Pu^{4+} versus U^{4+}. From analysis of the latter pair, we find that, for a given host lattice, UO_2 is somewhat less soluble than PuO_2 (compare figures 5.7 and 5.8 for simple solution, figures 5.9 and 5.10 for co-solution); this comes about because the ionic radius of U^{4+} is slightly larger than the radius of Pu^{4+} [174]. The result is useful since it gives some credence to the idea that data involving U^{4+} may provide a useful upper bound for the behaviour of Pu^{4+} (although the redox behaviour of U^{4+} is rather different to Pu^{4+}). Similarly by comparing figures 5.1 and 5.7 it can be seen that the solution energy for Pu^{3+} is always less than Pu^{4+}. This implies that it is possible to accommodate more Pu^{3+} ions than Pu^{4+} into the same amount of host matrix. If Pu^{3+} is incorporated and the conditions in the repository change so that these ions are oxidised into their 4+ state then this would cause problems as the matrix will become supersaturated with Pu^{4+} and segregation would begin to occur. The most likely destination for the excess Pu^{4+} ions would be the grain boundaries and surfaces of the material, which would increase the rate of leaching of plutonium from the material. Finally, it was shown that these simulations are consistent with co-solution providing energetically favourable solution mechanisms (although more work is required with respect to the Ca^{2+} mediated reaction to include the more complex zirconolite phases and calculations of U^{5+} explicitly).